Experimental and numerical investigation of compressibility effects on velocity derivative flatness in turbulence

K. Yamamoto (山本 航平), **T. Ishida** (石田 竜也), **T. Watanabe** (渡邉 智昭), **et al.**

View Online   Export Citation   CrossMark

Experimental and numerical investigation of compressibility effects on velocity derivative flatness in turbulence

K. Yamamoto (山本 航平),[1] T. Ishida (石田 竜也),[2] T. Watanabe (渡邉 智昭),[3,a] (iD) and K. Nagata (長田 孝二)[1] (iD)

AFFILIATIONS

[1]Department of Aerospace Engineering, Nagoya University, Furo-cho, Chikusa, Nagoya 464-8603, Japan
[2]Undergraduate Department of Mechanical and Aerospace Engineering, Nagoya University, Furo-cho, Chikusa, Nagoya 464-8603, Japan
[3]Education and Research Center for Flight Engineering, Nagoya University, Furo-cho, Chikusa, Nagoya 464-8603, Japan

[a]Author to whom correspondence should be addressed: watanabe.tomoaki@c.nagoya-u.jp

ABSTRACT

Compressibility effects on the velocity derivative flatness $F_{\partial u'/\partial x}$ are investigated by experiments with opposing arrays of piston-driven synthetic jet actuators (PSJAs) and direct numerical simulations (DNS) of statistically steady compressible isotropic turbulence and temporally evolving turbulent planar jets with subsonic or supersonic jet velocities. Experiments using particle image velocimetry show that nearly homogeneous isotropic turbulence is generated at the center of a closed box from interactions between supersonic synthetic jets. The dependencies of $F_{\partial u'/\partial x}$ on the turbulent Reynolds number Re_λ and the turbulent Mach number M_T are examined both experimentally and using DNS. Previous studies of incompressible turbulence indicate a universal relationship between $F_{\partial u'/\partial x}$ and Re_λ. However, both experiments and DNS confirm that $F_{\partial u'/\partial x}$ increases relative to the incompressible turbulence via compressibility effects. Although $F_{\partial u'/\partial x}$ tends to be larger with M_T in each flow, the $F_{\partial u'/\partial x}$ in the turbulent jets and the turbulence generated from PSJAs deviate from those in incompressible turbulence at lower M_T compared with isotropic turbulence sustained by a solenoidal forcing. The PSJAs and supersonic planar jets generate strong pressure waves, and the wave propagation can cause an increased $F_{\partial u'/\partial x}$, even at low M_T. These results suggest that the compressibility effects on $F_{\partial u'/\partial x}$ are not solely determined from a local value of M_T and depend on the turbulence generation process.

Published under an exclusive license by AIP Publishing. https://doi.org/10.1063/5.0085423

I. INTRODUCTION

Compressible turbulence generated in high-speed flows is an important phenomenon in various scientific fields. In aerospace engineering, turbulent boundary layers develop in high-speed flows on aircraft surfaces.[1] Turbulence that evolves under strong compressibility effects is also encountered in propulsion systems,[2,3] where turbulence can enhance the mixing of heat and substances, which affects the overall system performance. Compressible turbulence has also been studied in astrophysics due to its relevance in star formation.[4,5]

Fundamental studies of turbulence often consider canonical flows, such as isotropic turbulence, free shear flows, and boundary layers on flat plates. Such low-speed and incompressible flows have been studied both experimentally and through direct numerical simulations (DNS).[6] It is widely considered in incompressible turbulence that the statistical properties of small-scale turbulent motion have some universal characteristics that do not depend on the flow type.

Most small-scale quantities are defined with a velocity gradient tensor $\partial u_i / \partial x_j$. Both experimental and numerical studies of incompressible turbulence indicate that the relationship between the velocity derivative flatness and turbulent Reynolds number $Re_\lambda = u_{rms}\lambda/\nu$ barely differs between flows,[7] where u_{rms} is the root mean square (rms) of the velocity fluctuations, λ is the Taylor microscale, and ν is the kinematic viscosity. Previous DNS studies have reported that the compressibility effects can alter the small-scale universality of turbulent flow. For example, the skewness and flatness of the velocity derivative change as the compressibility effects strengthen.[8,9]

One important parameter of compressible turbulence is the turbulent Mach number $M_T = \sqrt{u_{rms}^2 + v_{rms}^2 + w_{rms}^2}/a$, where v_{rms} and w_{rms} are the rms velocity fluctuations in the y and z directions and a is the speed of sound. Many publications have considered M_T as the dominant parameter that determines the compressibility effects on the turbulence.[10–24] Therefore, the M_T scalings for various quantities have

been explored in previous studies. Statistics related to small-scale turbulent motion tend to differ greater between compressible and incompressible turbulence for larger M_T.[9,25] Donzis and John examined DNS data for statistically steady isotropic turbulence with various forcing schemes.[8] They showed that the compressibility effects on turbulence differ for dilatational and solenoidal forcing schemes, even for the same M_T. Their analyses suggest that the compressibility effects can be significant when force is applied to the dilatational velocity component, even at $M_T = \mathcal{O}(10^{-2})$. However, the assumption of incompressibility is valid for isotropic turbulence with $M_T = \mathcal{O}(10^{-2})$ if the turbulence is subject to solenoidal forcing.[8,9] These DNS results indicate that the compressibility effects on forced isotropic turbulence depend on how the turbulence is sustained. However, most numerical simulations of forced compressible isotropic turbulence have employed artificial forcing schemes that input energy selectively into solenoidal or dilatational velocity components,[5,9,19,24,26] although such a selective mechanism to generate turbulence may not be valid for realistic flows. Therefore, it is unclear whether such numerical observations based on artificial forcing are consistent with turbulent flows generated in the laboratory. Furthermore, DNS often deals with shock waves using shock-capturing schemes, which numerically smooth quasi-discontinuous shock waves.[27] Such issues in numerical studies make it important to investigate compressible turbulence generated by various methods both experimentally and using numerical simulations.

In laboratory experiments, nearly homogeneous isotropic turbulence is often generated in wind tunnel experiments by installing a grid at the entrance of the test sections.[22,28–32] Experiments on compressible turbulence have also been performed for grid turbulence generated in shock tube facilities and supersonic or transonic wind tunnels.[33–35] Another example of compressible turbulence experiments is the variable density and speed of the sound vessel, where compressible turbulence is generated using heavy gases.[36] Some studies have considered the effects of turbulence on shock wave propagation.[37,38] However, the characteristics of grid turbulence generated in high-speed flows have been investigated less than subsonic flows. Other facilities to generate incompressible homogeneous isotropic turbulence have also been developed in recent decades. One example is a closed turbulence chamber in which stirring devices generate turbulence. Turbulence chambers are often developed using synthetic jet actuators, which are equipped on the internal surface of the chamber.[39,40] Electrical fans have also been used in turbulence chambers, where flow interactions induced from the fans generate nearly homogeneous isotropic turbulence.[41–43] Interactions between continuous or pulse-operated jets have also been used to generate turbulence with desired properties.[44–47]

Turbulence chambers are useful for experimental investigations of compressible turbulence as the instantaneous velocity is as large as the velocity fluctuations, while the turbulence generated in high-speed wind tunnels has an instantaneous velocity that is much larger than the fluctuations. However, most turbulence chambers produce incompressible turbulence because stirring devices induce subsonic flows. Recently, we developed a novel turbulence chamber that generates compressible turbulence from interactions between many high-speed synthetic jets.[48] This facility utilizes piston-driven synthetic jet actuators (PSJAs)[49–52] to induce supersonic flow in a closed chamber. Opposing arrays of PSJAs can generate statistically steady and nearly homogeneous isotropic turbulence with a small mean velocity at the chamber center. The employment of PSJAs extends the velocity range

of turbulence chambers from subsonic to transonic and even supersonic regimes. Furthermore, the ability of PSJAs to generate statistically steady turbulence helps evaluate flow statistics and take measurements for a long time without limitations from the time duration of the facility. As discussed above, DNS studies have shown that the compressibility effects on turbulence depend on the forcing schemes, and a comparison of compressible turbulence generated by different methods is important. Therefore, the turbulence chamber equipped with PSJAs can provide unique data for compressible turbulence to reveal the universality and flow dependence of the compressibility effects on turbulence.

Our previous study of the turbulence chamber with PSJAs reported the fundamental properties of turbulent flow as induced in the chamber.[48] It is of interest to investigate the compressibility effects on small-scale characteristics of turbulence, whose universality reported for incompressible turbulence may not be realized in compressible turbulence. This study reports experiments of turbulence as generated from PSJAs using particle image velocimetry (PIV) and Schlieren flow visualization. The experimental data are examined to investigate the relationship between the velocity derivative flatness with the turbulent Reynolds number and the turbulent Mach number. We also analyze the DNS database for two types of compressible turbulence: statistically steady isotropic turbulence subject to a solenoidal linear forcing[9] and temporally evolving turbulent planar jets.[53] Comparing the experiments using PSJAs with DNS provides experimental evidence that the compressibility effects on the small-scale characteristics of turbulence are not solely determined by the local turbulent Mach number.

The remainder of this paper is organized as follows. Section II describes the experiments of the turbulence chamber using PSJAs. Section III provides details of the DNS databases for isotropic turbulence and turbulent planar jets. The experimental and numerical results are discussed in Sec. IV. The fundamental characteristics of turbulence as generated from the PSJAs are presented in Sec. IV A. Then, Sec. IV B explores the compressibility effects on the velocity derivative flatness by comparing the experimental and numerical data. Section IV C discusses the compressibility effects based on wave propagation. Finally, the paper is summarized in Sec. V.

II. TURBULENCE EXPERIMENTS WITH PISTON-DRIVEN SYNTHETIC JET ACTUATORS

A. Turbulence chamber of piston-driven synthetic jet actuators

Experiments are performed with the turbulence chamber equipped with PSJAs.[48] The PSJAs are developed to generate synthetic jets with larger velocities than conventional synthetic jets, which are often generated via piezoelectrically driven diaphragms.[49–52] The details of the PSJAs used in this study are in Refs. 48 and 52. The PSJAs generate high-speed synthetic jets using a piston-cylinder actuator (model engine) as driven with a DC brushless motor. An interchangeable plate with a hole is equipped on the cylinder top. The piston movement is repeatedly driven by the motor to inject and eject air through the hole on the plate and generate the synthetic jet. The actuation frequency of the PSJA is adjusted with an electric speed controller (ESC) connected to the motor, while the rotational speed is measured with a magnet attached to the engine shaft and a magnetic sensor.

Figure 1 shows a photograph of the turbulence chamber. Eight PSJAs are installed on two opposite surfaces of a rectangular box with
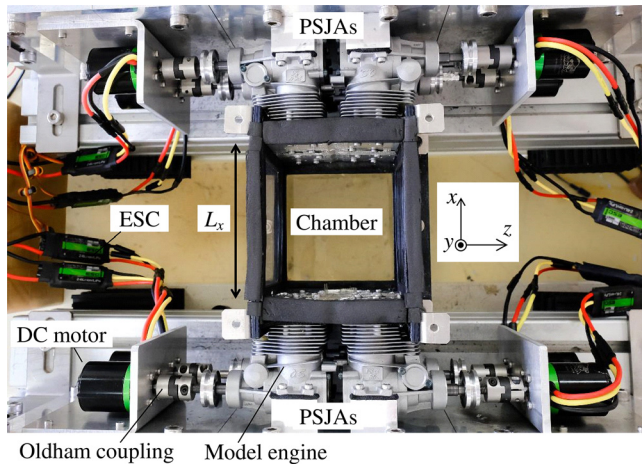
FIG. 1. Top view of the turbulence chamber with eight PSJAs equipped on opposite surfaces.

an arrangement on one surface shown in Fig. 2. A synthetic jet is generated from each PSJA from a simple sharp-edged orifice with a diameter of 4 mm and a length of 13 mm. The plates with the orifice holes are manufactured via stereolithography 3D printing with a printing resolution of approximately 10 μm. The experiments are conducted with an actuation frequency of $f = 150$ Hz. For this actuation frequency and hole diameter, the PSJAs generate supersonic flows with a maximum jet Mach number of approximately 1.2 in the blowing phase and subsonic flow in the suction phase.[52] The jets are repeatedly issued horizontally from each PSJA, and the jet interaction generates turbulence in the closed chamber. The initial phase of the pistons is unmatched between the eight PSJAs. The direction of the jet is denoted by x, while the vertical and spanwise directions are denoted by y and z, respectively. The distance between the two surfaces with the PSJAs is denoted as L_x in Fig. 1. The chamber walls consist of four interchangeable plates that connect to the housing plates of the PSJAs.
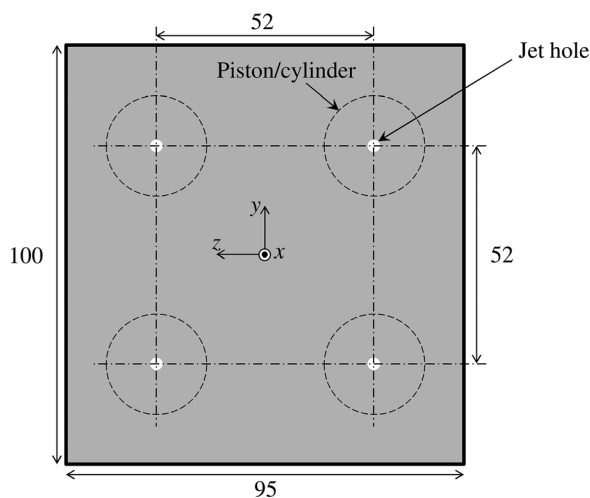

FIG. 2. Location of jet holes on one side of the turbulence chamber with all dimensions in mm.

The side and bottom walls of the chamber are glass, and the top wall is acrylic. The chamber walls can be exchanged to vary L_x. The experiments are conducted with $L_x = 110$ and 220 mm, which are denoted as exps. 1 and 2, respectively. The side length of the chamber is 100 mm in the y direction and 95 mm in the z direction. The origin of the coordinate system is located at the chamber center.

B. Measurement methods

A two-dimensional and two-component (2D2C) PIV system (Dantec Dynamics) is used to measure velocity vectors (u and v) on the x-y plane around the chamber center. The same PIV system was also used in Ref. 48. The measurement area of the PIV is -15 mm $\leq x \leq 15$ mm and -9 mm $\leq y \leq 9$ mm at $z = 0$. The PIV system consists of a double-pulse Nd:YAG laser (Dantec Dynamics, Dual Power 65–15) and a high-speed camera (Dantec Dynamics, SpeedSense 9070). A camera lens with a focal length of 60 mm (Nikkon, Ai AF Micro-Nikkor 60 mm f/2.8D) is connected to the camera through an extension tube to increase the magnification factor and achieve a high spatial resolution. The laser system is equipped with light sheet optics to produce a laser sheet with a thickness smaller than 1 mm. Oil mist is used as tracer particles, which are illuminated by two laser pulses at an interval of 2.5 μs. The oil mist is seeded in the chamber by condensation of engine oil, which is evaporated in the cylinder due to a temperature increase by fluid compression.[48] Pairs of particle images are recorded in two frames by the camera and analyzed with an adaptive PIV algorithm implemented in Dantec Dynamic Studio. Most of the results are presented for the velocity vectors obtained with an interrogation window size of 32×32 pixels. The same conclusion can be reached by the data obtained with window sizes of 24^2 and 32^2 pixels, as shown in Sec. IV.

In each measurement, the camera starts to record 300 pairs of particle images 5 s after the PSJAs are turned on. During these 5 s, the jets eject from each PSJA approximately 750 times, which is enough for the turbulence to reach a statistically steady state.[48] The PIV measurements for each experimental condition are repeated 5 times for exp. 1 and 10 times for exp. 2. The results of exp. 2 are also used to quantify the statistical errors. The sampling rate is 15 Hz, which gives a sampling interval longer than the eddy turnover time of the turbulence. Therefore, each vector image represents an independent snapshot of the flow. The statistics are evaluated with ensemble averages. For N vector images, an average of a variable $f(x, y)$ is calculated as $\langle f \rangle (x, y) = (1/N) \Sigma_{n=1}^{N} f^{(n)}(x, y)$, where the superscript (n) represents the nth image. The rms fluctuations of f are defined as $f_{rms} = \sqrt{\langle f'^2 \rangle}$ with $f' = f - \langle f \rangle$. The spatial resolution $\Delta \approx 0.5$ mm on the measurement plane is about 8 times the Kolmogorov scale $\eta = \nu^{3/4} \varepsilon^{-1/4}$, where ν is the kinematic viscosity at the temperature T in the chamber, while the kinetic energy dissipation rate ε is estimated as $\varepsilon = 15\nu \langle (\partial u/\partial x)^2 \rangle$.

Flow visualization is also performed using the Schlieren technique. A schematic of the Schlieren system is shown in Fig. 3. A point light from a Xenon lamp is collimated using an achromatic lens with a focal length of 500 mm. The collimated light passes through the chamber in the z direction and is recorded by the camera after passing another achromatic lens with a focal length of 800 mm and a knife-edge. The Schlieren visualization uses a high-speed camera (Dantec
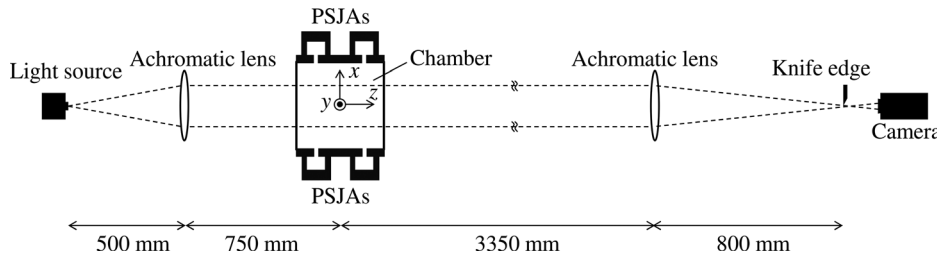
FIG. 3. Optical setup for the Schlieren flow visualization.

Dynamics, Speed Sense 9072) with settings presented when the images are shown in Sec. IV.

III. DIRECT NUMERICAL SIMULATIONS OF STATISTICALLY STEADY ISOTROPIC TURBULENCE AND TEMPORALLY EVOLVING PLANAR JETS

The experimental results are compared with the DNS of statistically steady homogeneous isotropic turbulence and temporally evolving turbulent planar jets. The flows were investigated in our previous papers.[9,53,54] Here, we briefly describe the DNS of the flows, and further details of the flow characteristics are found in Refs. 9, 53, and 54, where the simulations were validated by comparison with other experimental and numerical studies.

The governing equations are the compressible Navier–Stokes equations and the equation of state for an ideal gas, which are given as

$$\frac{\partial \rho}{\partial t} + \frac{\partial \rho u_j}{\partial x_j} = 0, \tag{1}$$

$$\frac{\partial \rho u_i}{\partial t} + \frac{\partial \rho u_i u_j}{\partial x_j} = -\frac{\partial P}{\partial x_i} + \frac{\partial \tau_{ij}}{\partial x_j}, \tag{2}$$

$$c_v \frac{\partial \rho T}{\partial t} + c_v \frac{\partial \rho T u_j}{\partial x_j} = -P\frac{\partial u_j}{\partial x_j} + \frac{\partial}{\partial x_j}\left(\kappa \frac{\partial T}{\partial x_j}\right) + \tau_{ij}\frac{\partial u_i}{\partial x_j}, \tag{3}$$

$$P = \rho R T, \tag{4}$$

with the viscous stress tensor τ_{ij} given by

$$\tau_{ij} = \mu\left(\frac{\partial u_i}{\partial x_j} + \frac{\partial u_j}{\partial x_i} - \frac{2}{3}\delta_{ij}\frac{\partial u_k}{\partial x_k}\right). \tag{5}$$

Here, ρ is the density, u_i is the velocity vector, P is the pressure, T is the temperature, μ is the viscosity coefficient, κ is the thermal conductivity, and δ_{ij} is the Kronecker delta function. We assume the working gas is air. The gas constant R is related to the specific heat capacity at a constant pressure (c_p) and constant volume (c_v) by $R = c_p - c_v = 287$ J/(kg K), while the specific heat ratio is $\gamma = c_p/c_v = 1.4$. The viscosity μ is calculated as a function of temperature using Sutherland's law. The Prandtl number $Pr = \mu c_p/\kappa$ is 0.71.

A. Statistically steady isotropic turbulence sustained by solenoidal linear forcing

Statistically steady compressible isotropic turbulence is simulated in a triply periodic box. The statistically steady state is achieved using the solenoidal linear forcing scheme.[9] Herein, the forcing and cooling terms are added to Eqs. (2) and (3). The flow conditions are determined by specifying the steady-state values of the Reynolds number

Re_{L0}, the turbulent Mach number M_{T0}, the mean pressure P_0, and the mean temperature T_0. Here, $Re_{L0} = \rho_0 u_0 L_0/\mu_0$ and $M_{T0} = \sqrt{3}u_0/a_0$ are defined using the rms velocity fluctuations u_0, the integral length scale $L_0 = u_0^3/\varepsilon_0$ (ε_0 is turbulent kinetic energy dissipation rate per unit mass), and the density (ρ_0), viscosity (μ_0), and speed of sound (a_0) corresponding to P_0 and T_0. All simulations are performed for $P_0 = 101.3$ kPa and $T_0 = 300$ K, while $Re_{L0} = 350$ and 900 and $M_{T0} = 0.3, 0.4,\ldots, 0.9$. The shocklets are generated when $M_{T0} \gtrsim 0.6$ for the present forcing scheme.[9] The size of the computational domain is $(L_x, L_y, L_z) = (5.5L_0, 5.5L_0, 5.5L_0)$, and simulations for $Re_{L0} = 350$ have been reported in a previous paper,[9] while those with $Re_{L0} = 900$ are conducted for this study.

The governing equations are temporally integrated with a third-order total variation diminishing Runge–Kutta scheme.[55] Turbulence at high M_{T0} generates shocklets where a fluid is significantly compressed and physical variables exhibit quasi-discontinuous jumps. To handle discontinuity across the shocklets, the inviscid terms (advection and pressure) near the shocklets are computed using the hybrid scheme that utilizes the sixth-order central difference scheme and fifth-order weighted essentially non-oscillatory (WENO) scheme combined with the advection upstream splitting method (AUSM).[27,56] The former is applied for smooth regions, while the latter is for highly compressive regions, which are defined as $\theta \equiv \partial u_j/\partial x_j < -5\theta_{rms}$, where θ_{rms} is the rms fluctuations of the dilatation θ. The explicit tenth-order low-pass filter in Ref. 57 is applied to ρ, ρu_i, and ρT at the end of each time step to maintain numerical stability as the central difference scheme is used in most regions.[58]

For statistically steady isotropic turbulence, the statistics are defined with averages computed as a volume average in the computational domain and a time average. Here, the time average is taken as 20 times the eddy turnover time, L_0/u_0. The average is denoted as $\langle * \rangle$, which does not depend on the position or time. The computational grid is uniform in three directions, and the numbers of grid points are $(N_x, N_y, N_z) = (768, 768, 768)$ for $Re_{L0} = 350$ and $(1536, 1536, 1536)$ for $Re_{L0} = 900$. The spatial resolution $\Delta = L_x/N_x$ is approximately 0.8 times the Kolmogorov scale η. Here, η is defined as $\eta = (\langle\mu\rangle/\langle\rho\rangle)^{3/4}\varepsilon^{-1/4}$ with the kinetic energy dissipation rate $\varepsilon = \langle\tau_{ij}S_{ij}\rangle/\langle\rho\rangle$, where S_{ij} is the rate-of-strain tensor.

B. Temporally evolving planar jets

The DNS database of the temporally evolving planar jets is the same as in Refs. 53 and 54. The computational domain is periodic in both the streamwise (x) and spanwise (z) directions. The lateral direction of the planar jet is denoted by y. The jet develops in the y direction with time from the initial condition. The statistics are defined with an average $\langle * \rangle$ taken in the x and z directions as functions of y and time.

The initial mean streamwise velocity is given by $\langle u \rangle = U_J/2 + (U_J/2)\tanh[(H - 2|y|)/4\theta_J]$, while the mean velocities in the other directions are zero. Here, $y = 0$ is at the center of the planar jet, U_J is the jet velocity, H is the jet width, and $\theta_J = 0.03H$ is the shear layer thickness at the jet edges. The initial pressure is 101.3 kPa, which is uniform in space. The initial temperature is 300 K except at the jet edges, where the temperature profile is given by the Crocco–Busemann relation.[59] The parameters U_J and H are determined by choosing the Reynolds number $Re_J = \rho_J U_J H/\mu_J$ and the Mach number $M_J = U_J/a_J$, where ρ_J, μ_J, and a_J are the density, viscosity, and speed of sound in the jet at the initial state. This study uses the DNS database with $(Re_J, M_J) = (14\,000, 0.6)$, $(14\,000, 1.6)$, and $(14\,000, 2.6)$. All DNS were conducted with the computational domain of $(L_x, L_y, L_z) = (12H, 30H, 6H)$. The numbers of grid points are $(N_x, N_y, N_z) = (2200, 1400, 1100)$. The grid spacing is uniform in the x and z directions, while the grid size in the y direction is refined near the jet centerline using a mapping function based on a hyperbolic tangent function.[53] The DNS code is based on fully explicit finite difference schemes, which have been detailed in previous papers.[53,54,60] We analyze the flow fields at non-dimensional times of $t/t_r = 18$ and 26 ($t_r = H/U_J$), which are in the fully developed and self-similar regime. At $t/t_r = 26$, the spatial resolution Δ on the jet centerline is 1.3η, 1.2η, and 1.0η, for $M_J = 0.6$, 1.6, and 2.6, respectively.

IV. RESULTS AND DISCUSSION

A. Fundamental characteristics of turbulence generated by PSJAs

The fundamental statistics of turbulence as generated by the PSJAs are presented here, while the statistical properties of isotropic turbulence and turbulent planar jets were documented in previous studies.[9,53,61,62] Figure 4 illustrates the instantaneous velocity vectors $\mathbf{u} = (u, v)$ for exp. 2. In this snapshot, the maximum velocity reaches approximately 15 m/s, and the jet holes are not at the measurement plane of the PIV. Therefore, synthetic jets are not visible on the velocity field. Figure 5 (Multimedia view) shows the Schlieren image taken near the chamber center in exp. 1. The framerate and exposure time in one frame are 8102 fps and 11 μs, respectively. At the top and bottom
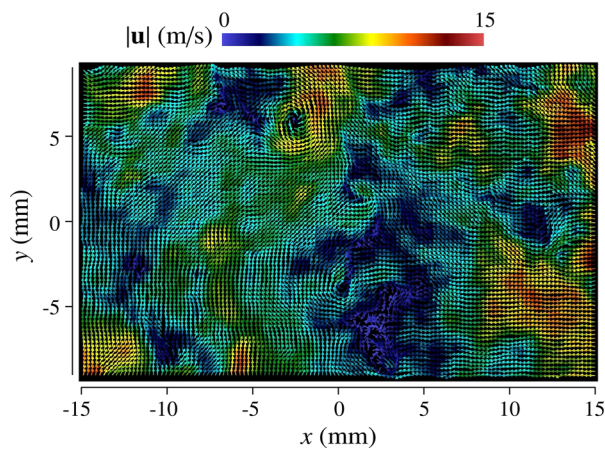

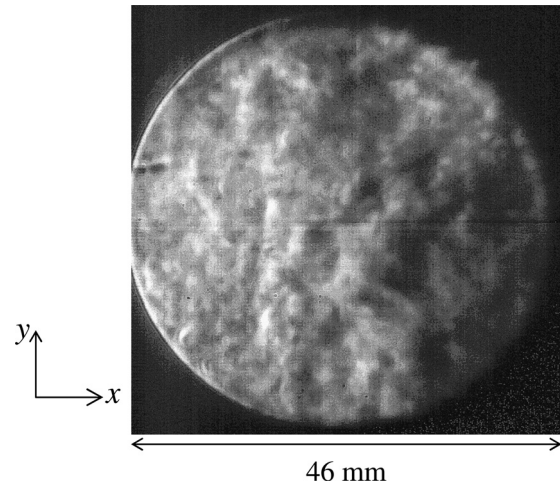FIG. 4. Instantaneous velocity vectors in exp. 2, where the color represents the velocity magnitude $|\mathbf{u}|$.

FIG. 5. Schlieren visualization of turbulence near the chamber center in exp. 1. Multimedia view: https://doi.org/10.1063/5.0085423.1.

of the visualized region, the jet flows in the $\pm x$ directions are repeatedly observed in the video. The Schlieren image contains the information integrated along the light path. Therefore, the jets are visualized even though the holes are not located on the x-y plane that crosses the chamber center, where the velocity is measured with the PIV. The mean flow of the jets does not appear on the central plane of the chamber.[48]

Table I summarizes the statistics at the center of the measurement area. The temperature T is measured using a K-type thermocouple (A&D, AD-5601A) 10 s after the PSJAs are turned on. The temperature in the chamber increases from room temperature due to the fluid compression in the PSJAs at the beginning of the experiments. However, T is nearly constant once turbulence has developed.[48] The mean velocities $(\langle u \rangle, \langle v \rangle)$ are smaller than 2 m/s, while the instantaneous velocity exceeds 10 m/s in Fig. 4. The rms velocity fluctuations, u_{rms} and v_{rms}, are 4–6 m/s. Thus, turbulence with a small mean velocity is generated around the chamber center. The ratio $u_{rms}/v_{rms} \approx 1$ in exp. 1 suggests that large-scale velocity fluctuations are isotropic near the chamber center. On the other hand, u_{rms}/v_{rms} is slightly larger than 1 in exp. 2 as it has a large chamber length. Table I also shows the turbulent Reynolds number Re_λ and the turbulent Mach number M_T. Here, $Re_\lambda = u_{rms}\lambda_x/\nu$ is calculated using the Taylor microscale $\lambda_x = u_{rms}/(\partial u/\partial x)_{rms}$, the kinematic viscosity of air at temperature T in Table I, and the atmospheric pressure. The turbulent Mach number is calculated as $M_T = \sqrt{u_{rms}^2 + 2v_{rms}^2}/a$ with the speed of sound a for T because $v_{rms} = w_{rms}$ is expected at the chamber center. The turbulence generated by the PSJAs has $Re_\lambda = \mathcal{O}(10^2)$. The difference in Re_λ between exps. 1 and 2 is caused primarily by a larger Taylor microscale in exp. 2. The length scales of a turbulent jet increase with the jet development. The larger length scale in exp. 2 is explained by the long distance from the jet exit to the measurement location. The turbulent Mach number is $\mathcal{O}(10^{-2})$ for both experiments, and the velocity fluctuations are subsonic at the chamber center. However, the velocity becomes supersonic near the jet hole,[52] and the generation of turbulence is strongly influenced by the compressibility effects.

TABLE I. Turbulence characteristics at the center of the measurement area.

	L_x (mm)	$\langle u \rangle$ (m/s)	$\langle v \rangle$ (m/s)	u_{rms} (m/s)	v_{rms} (m/s)	u_{rms}/v_{rms}	$\langle u \rangle/u_{rms}$	$\langle v \rangle/v_{rms}$	Re_λ	M_T
Exp. 1	110	0.51	−0.61	4.2	4.1	1.02	0.12	−0.14	383	0.019
Exp. 2	220	1.92	−0.33	5.8	4.8	1.21	0.33	−0.068	932	0.027

If the PSJAs have the same initial phase for the piston, jet ejection occurs simultaneously. The phase correlation may affect the interactions between synthetic jets. The PIV measurements to acquire 300 snapshots of the velocity profiles are repeated 10 times for exp. 2. The initial phases of the PSJAs differ in each PIV measurement. Therefore, a comparison between these repeated experiments helps examine the effects of the initial phase and phase correlation. Table II presents u_{rms} and v_{rms} at the chamber center for each measurement of exp. 2. Statistical errors due to the limited number of samples are not negligible for 300 snapshots. However, the results are qualitatively similar in all measurements, and u_{rms} is slightly larger than v_{rms}. When two opposed PSJAs operate with the same phase, strong collisions of the opposed jets may occur and induce large velocity fluctuations in the transverse direction of the jets. Then, v_{rms} can be larger than u_{rms}.[47] The results in Table II suggest that although such collisions due to this matched phase may occur, their influence is not significant enough to affect u_{rms}/v_{rms}. Our previous study with the same turbulence chamber also confirmed that the initial phase does not affect the mean velocity and rms velocity fluctuations for the off-center plane of the chamber.[48] Although the actuation frequency is set to $f = 150$ Hz, f slightly fluctuates during the experiments.[52] These fluctuations weaken the effects of phase correlations because the phase difference between PSJAs varies with time if f is not constant. Another issue related to the phase is the correlation with the PIV measurements. The velocity vectors are acquired at a frequency of 15 Hz, which is 1/10 the actuation frequency of the PSJAs. Therefore, the PIV may always capture images at specific phases of piston movement. However, this is not the case because of small fluctuations in the actuation frequency. If the phase were strongly correlated with the PIV sampling, the measurements performed for different initial phases would yield different results. As discussed above, the statistics barely differ, even if the initial phases are different. Therefore, the influence of the sampling rate can be negligible in the present experiments.

Table II suggests that statistical errors due to the finite number of samples are negligible when 1500 snapshots are used to evaluate the statistics. The averages calculated separately for runs 1–5 and 6–10 yield $(u_{rms}, v_{rms}) = (5.86, 4.68$ m/s$)$ and $(5.84, 4.76$ m/s$)$, respectively. These values differ from the averages of runs 1–10 by less than
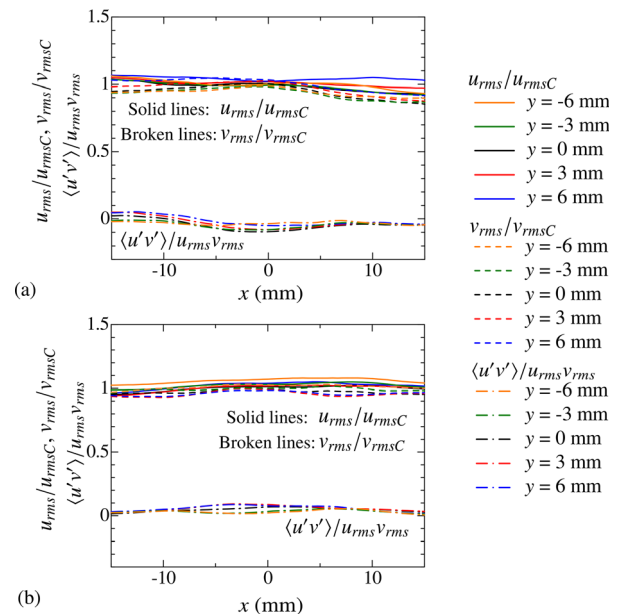
1%. Therefore, using more than 1500 snapshots in the statistical analysis barely changes the results in this paper.

Figure 6 shows the lateral profiles of u_{rms}, v_{rms}, and the correlation coefficient between u and v defined as $\langle u'v' \rangle/u_{rms}v_{rms}$ in exps. 1 and 2. In the measurement area, u_{rms} and v_{rms} barely vary in space as their spatial variations are less than 15% of the values at the chamber center. Furthermore, the measurement area has $|\langle u'v' \rangle/u_{rms}v_{rms}| \lesssim 0.1$. The correlation is expected to be large inside the synthetic jets because of the mean velocity gradient. A small $|\langle u'v' \rangle/u_{rms}v_{rms}|$ suggests that the chamber center is not directly affected by the mean flow of the synthetic jets and is dominated by turbulence generated by their interactions, which is more isotropic and homogeneous than synthetic jets.

Even if large-scale motion in turbulence is slightly anisotropic in exp. 2 as attested by $u_{rms}/v_{rms} > 1$, small-scale motion can be locally isotropic. This local isotropy is often investigated with statistics for the velocity derivatives.[63–65] In this study, the local isotropy at small scales is examined using rms fluctuations of the velocity derivative, $(\partial u_i/\partial x_j)_{rms}$. Figure 7 plots $(\partial u/\partial x)_{rms}/(\partial v/\partial y)_{rms}$ and $(\partial u/\partial y)_{rms}/(\partial v/\partial x)_{rms}$ as functions of Re_λ. The experimental results for the PSJAs are compared with the DNS of the planar jets. These ratios are

TABLE II. Root-mean-squared velocity fluctuations, u_{rms} and v_{rms}, at the chamber center as obtained in each measurement for exp. 2.

Run	1	2	3	4	5	6	7	8	9	10
u_{rms} (m/s)	5.71	5.94	6.09	5.97	5.61	5.86	5.74	5.80	5.69	6.09
v_{rms} (m/s)	4.60	4.72	4.73	4.58	4.78	4.77	4.57	5.11	4.74	4.61
u_{rms}/v_{rms}	1.24	1.26	1.29	1.30	1.17	1.23	1.26	1.14	1.20	1.32

FIG. 6. Lateral profiles of the rms velocity fluctuations u_{rms} and v_{rms} and correlation coefficient $\langle u'v' \rangle/u_{rms}v_{rms}$ at $y = \pm6, \pm3$, and 0 mm in (a) exp. 1 and (b) exp. 2. The u_{rms} and v_{rms} at the chamber center are denoted by u_{rmsC} and v_{rmsC} and are used for normalization.
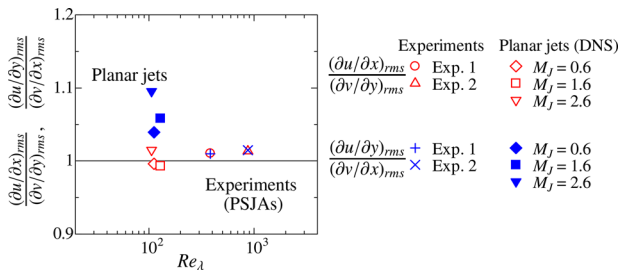
FIG. 7. The Re_λ dependence of the ratios of the rms fluctuations for the velocity derivatives, $(\partial u/\partial x)_{rms}/(\partial v/\partial y)_{rms}$ and $(\partial u/\partial y)_{rms}/(\partial v/\partial x)_{rms}$. The horizontal line indicates the isotropic value of 1.

equal to 1 when the turbulence is locally isotropic. The turbulence generated by the PSJAs has $(\partial u/\partial x)_{rms}/(\partial v/\partial y)_{rms} \approx (\partial u/\partial y)_{rms}/(\partial v/\partial x)_{rms} \approx 1.01$, which are close to the isotropic value. Thus, the assumption of local isotropy is valid at the chamber center for both experiments. The turbulent planar jets also have $(\partial u/\partial x)_{rms}/(\partial v/\partial y)_{rms} \approx 0.99$–$1.01$ and $(\partial u/\partial y)_{rms}/(\partial v/\partial x)_{rms} \approx 1.04$–$1.10$, which are close to 1.

B. Reynolds number and Mach number dependence of velocity derivative flatness

Both experimental and numerical studies of incompressible turbulence indicate that the relationship between the velocity derivative flatness, $F_{\partial u'/\partial x} = \langle(\partial u'/\partial x)^4\rangle/\langle(\partial u'/\partial x)^2\rangle^2$, and turbulent Reynolds number Re_λ barely differs between flows. Here, the Re_λ and M_T dependences of $F_{\partial u'/\partial x}$ are examined with the experimental and numerical results for compressible turbulence. Figure 8 plots $F_{\partial u'/\partial x}$ as a function of Re_λ and compares the present experiments and DNS with previous studies of incompressible turbulence. In incompressible turbulence, $F_{\partial u'/\partial x}$ increases monotonically with Re_λ, where all data points for incompressible turbulence follow the same trend. Although the data for incompressible turbulence collapse well, $F_{\partial u'/\partial x}$ in the PSJA experiments and the DNS at high Mach numbers are larger than those in incompressible turbulence at similar Re_λ values. For isotropic turbulence with both $Re_{L0} = 350$ and 900, the deviation from the

values in incompressible turbulence becomes clear for $M_T \gtrsim 0.8$. The planar jet with $M_J = 2.6$ also has a larger $F_{\partial u'/\partial x}$ than those with $M_J = 0.6$ and 1.6 for which $F_{\partial u'/\partial x}$ is close to the data of incompressible turbulence. In the PSJA experiments, $F_{\partial u'/\partial x}$ is approximately 1.4–2.0 times larger than those in incompressible turbulence at similar Re_λ. Similarly, $F_{\partial u'/\partial x}$ in the planar jet with $M_J = 2.6$ is approximately 1.8 times higher than those at $M_J = 0.6$ and 1.6. Thus, the relative deviation from incompressible turbulence is similar in the PSJA experiments and the DNS of planar jets. Furthermore, $F_{\partial u'/\partial x}$ as measured for the PSJAs is larger for greater Re_λ. This tendency also agrees with compressible isotropic turbulence, where $F_{\partial u'/\partial x}$ increases with Re_λ for the same M_T.

We performed an additional experiment with the present PIV system for incompressible turbulence generated by many DC fans to examine the measurement accuracy. The multi-fan turbulence chamber is described in Appendix. A total of 182 fans are equipped on opposed surfaces of a rectangular chamber to generate turbulence by interactions between fan-induced flows. Each fan induces a flow with a mean velocity of approximately 10 m/s.[73] Nearly isotropic turbulence is generated at the chamber center. Both the PSJAs and fans generate turbulence with $Re_\lambda = \mathcal{O}(10^2)$. The relationship between $F_{\partial u'/\partial x}$ and Re_λ in the fan-generated turbulence is shown as the red-filled circle in Fig. 8. The results quantitatively agree with previous studies of incompressible turbulence. This comparison demonstrates that the measurements are accurate enough to discuss the compressibility effects on $F_{\partial u'/\partial x}$.

The statistics are computed with 1500 independent snapshots of (u, v) for exp. 1, while exp. 2 uses 3000 snapshots. The statistical convergence may affect the findings for the compressibility effect on $F_{\partial u'/\partial x}$. To evaluate the influence of statistical convergence, we divide the 3000 snapshots of exp. 2 into two groups of 1500 snapshots and calculate the statistics in each group. The $F_{\partial u'/\partial x}$ as calculated from 1500 snapshots differs by 5.8% from that to 3000 snapshots. The error bars in Fig. 8 show variations of 5.8% for exps. 1 and 2, which represent possible errors due to statistical convergence. The range of the error bars is smaller than the difference between the experiments and the data of incompressible turbulence, and the statistical error does not affect the discussion given here. Another issue in computing $F_{\partial u'/\partial x}$ is the spatial resolution of PIV. The interrogation window size
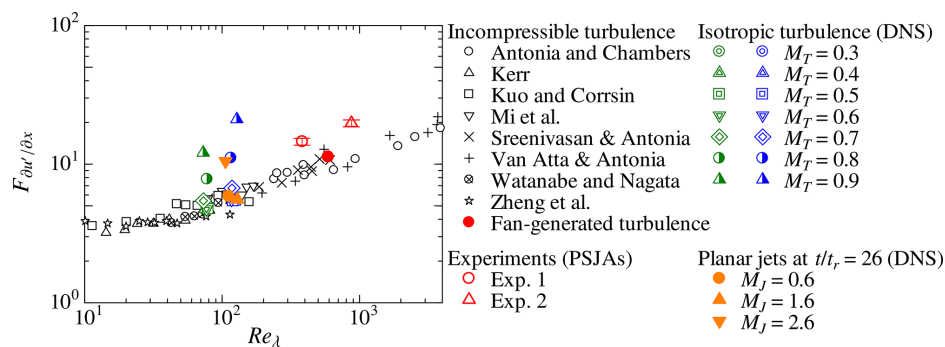

FIG. 8. Dependence of the velocity derivative flatness, $F_{\partial u'/\partial x}$, on the turbulent Reynolds number Re_λ. For experiments with PSJAs, $F_{\partial u'/\partial x}$ is shown at the chamber center. The error bars of exps. 1 and 2 show the ranges of 5.8% for $F_{\partial u'/\partial x}$, which represent possible errors due to the finite number of statistical samples. The experimental result for fan-generated turbulence as described in Appendix is shown to assess the measurement accuracy. The DNS results for the planar jets are taken on the jet centerline ($y = 0$) at $t/t_r = 26$. Data for incompressible turbulence[7,66–72] are also shown for comparison.
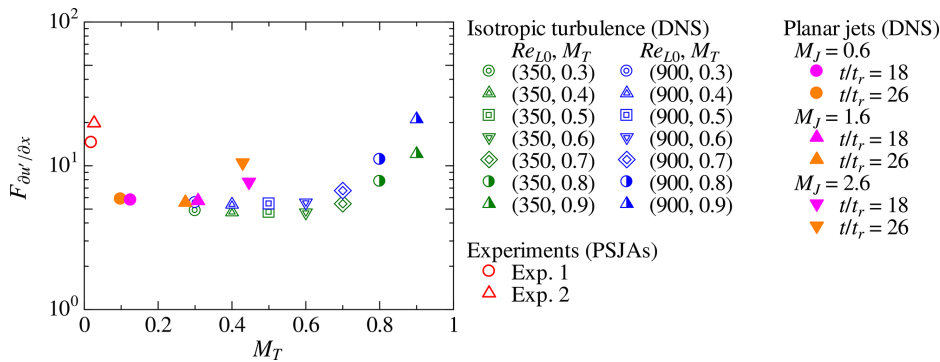
FIG. 9. Dependence of the velocity derivative flatness $F_{\partial u'/\partial x}$ on the turbulent Mach number M_T. The DNS results for the planar jets are taken at the jet centerline ($y = 0$) with $t/t_r = 18$ and 26, while the data for the experiments and compressible isotropic turbulence are the same as in Fig. 8.

used in the adaptive PIV algorithm is related to the resolution in the x-y plane. The results here are obtained with a window size of 32×32 pixels. Furthermore, $F_{\partial u'/\partial x}$ is computed with a different window size of 24×24 pixels, which are 1.5 times smaller than the original size. The $F_{\partial u'/\partial x}$ with 24×24 pixels is 9% larger than that for 32×32 pixels. Therefore, variations in $F_{\partial u'/\partial x}$ with the spatial resolution are small and the same compressibility effect on $F_{\partial u'/\partial x}$ is observed regardless of the interrogation window size.

The accuracy to evaluate $F_{\partial u'/\partial x}$ in DNS depends on the numerical schemes. The present DNS codes use high-order finite difference schemes for which the numerical solutions of the governing equations are accurate if the spatial resolution Δ is as small as the Kolmogorov scale η. The DNSs of the isotropic turbulence and the planar jets are performed using $\Delta/\eta \approx 0.8$ and $\Delta/\eta = 1.0$–1.3, respectively. The resolution is as good as those in previous DNS studies for the statistics of a velocity gradient tensor in compressible turbulent mixing layers.[74] Therefore, the velocity derivative statistics including the flatness are expected to be accurately evaluated in DNS. Figure 8 shows that the DNS results at low-Mach-number cases quantitatively agree with previous studies of incompressible turbulence.

The relation between $F_{\partial u'/\partial x}$ and Re_λ is well known for incompressible turbulence for which the accuracy of evaluating $F_{\partial u'/\partial x}$ can be easily assessed. However, $F_{\partial u'/\partial x}$ in compressible turbulence has rarely been considered, and it is difficult to compare the present results for compressible turbulence with existing works. Qualitatively, the same effect of flow compressibility on $F_{\partial u'/\partial x}$ is observed in the DNS and experiments for three different flows as $F_{\partial u'/\partial x}$ is larger than in incompressible flow. Therefore, the DNS and experiments conducted here

validate each other, which suggests the compressibility effects on $F_{\partial u'/\partial x}$ are not influenced by the accuracy of measurements and simulations.

Figure 9 plots $F_{\partial u'/\partial x}$ as a function of M_T for the experiments and DNS. For isotropic turbulence with both Reynolds numbers, $F_{\partial u'/\partial x}$ increases with M_T for $M_T \gtrsim 0.6$. However, deviations from the incompressible flows already occur at $M_T \approx 0.4$ for the planar jets. Once the turbulent jet has fully developed, M_T decays with time. For planar jets with $M_J = 2.6$, $F_{\partial u'/\partial x}$ increases from $t/t_r = 18$ to 26 even though M_T decreases over time. The experimental results for the PSJAs suggest that $F_{\partial u'/\partial x}$ can be larger than incompressible turbulence, even at $M_T = \mathcal{O}(10^{-2})$, for which $F_{\partial u'/\partial x}$ in the isotropic turbulence is close to those for incompressible turbulence. Thus, the compressibility effects on $F_{\partial u'/\partial x}$ are not determined solely by M_T.

The failure in describing the compressibility effects on $F_{\partial u'/\partial x}$ with M_T may be explained by the localness of M_T, which is defined at a given position or time in the flow. For example, the turbulent transition of a planar jet at a high M_J is significantly affected by the compressibility, even though M_T decreases as the fully developed turbulent jet evolves. The generation of turbulence by the PSJAs is also influenced by compressibility as the PSJAs generate supersonic synthetic jets. These compressibility effects on the generation process of turbulence are not well described using a local value of M_T in fully developed turbulence.

C. Flow dependence of the compressibility effects

In the PSJA experiments, $F_{\partial u'/\partial x}$ is larger than that in incompressible turbulence even though $M_T = \mathcal{O}(10^{-2})$ is not large. Similar compressibility effects at low M_T have been reported in DNS for forced
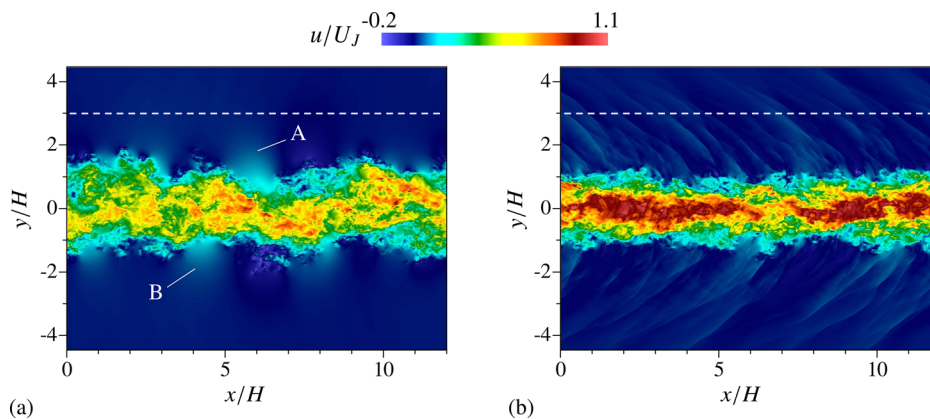

FIG. 10. Instantaneous streamwise velocity profiles at $t/t_r = 18$ on an x-y plane for planar jets with (a) $M_J = 0.6$ and (b) $M_J = 2.6$. The white line represents the location of $y/H = 3$ at which the probability density function of $\partial u'/\partial x$ in Fig. 12 is calculated.
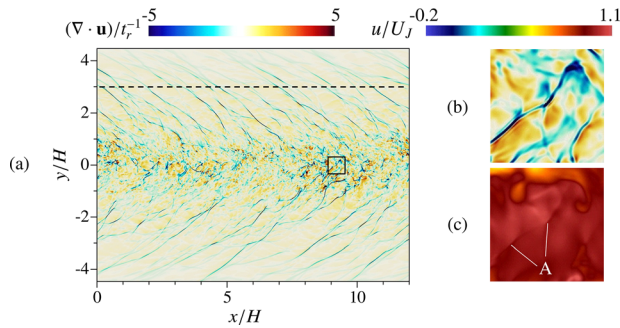
FIG. 11. (a) Instantaneous profile of dilatation $\theta = \partial u_j/\partial x_j$ at $t/t_r = 18$ on the x-y plane in the planar jet with $M_J = 2.6$. Profiles for (b) dilatation θ and (c) streamwise velocity u in the region outlined by the lines in (a). A broken line in (a) shows the location of $y/H = 3$.

FIG. 12. Probability density function of $\partial u'/\partial x$ at $y/H = 3$ in the planar jets ($t/t_r = 18$).

compressible isotropic turbulence.[8] They confirmed that deviations from incompressible turbulence occur for various statistics even at $M_T = \mathcal{O}(10^{-2})$ when forcing is applied to a dilatational velocity component. This study with PSJAs provides experimental support for their numerical findings of the compressibility effects at low M_T. The dilatational forcing scheme used in Ref. 8 results in the formation of shock-like compressive waves, even at low M_T. The strong compressive waves are accompanied by large velocity gradients inside the waves, which can increase the velocity derivative flatness. In the present experiments and DNS, $F_{\partial u'/\partial x}$ in the turbulent jets and the turbulence generated by the PSJAs deviate from incompressible turbulence at lower M_T rather than that in the isotropic turbulence generated by solenoidal forcing. The wave propagation is one of the probable reasons for the different threshold values of M_T that characterize deviation of $F_{\partial u'/\partial x}$ from incompressible turbulence. In isotropic turbulence with the present solenoidal forcing, the shocklets are observed for $M_T \gtrsim 0.6$.[9] The shock-like compressive waves are generated even for $M_T < 0.6$ in the turbulent planar jet as explained below. We also show that the synthetic jets via PSJAs generate pressure waves, which are strong enough to cause density fluctuations that are visible in the Schlieren images.

A supersonic jet is also known to generate strong pressure waves with a waveform similar to spherical shock.[75,76] Figure 10 illustrates two-dimensional profiles of the instantaneous streamwise velocity u in the planar jet at $M_J = 0.6$ and 2.6. The turbulent jet is located in
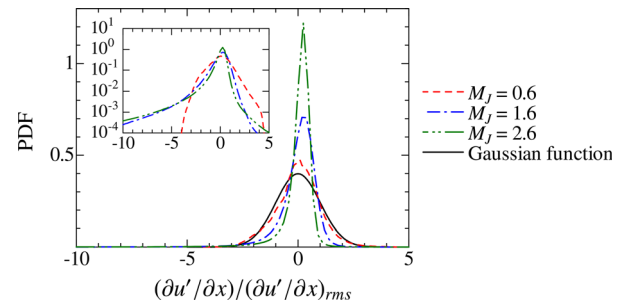
$|y/H| \lesssim 2$ for $M_J = 0.6$ and $|y/H| \lesssim 1$ for $M_J = 2.6$. A jet width at $M_J = 2.6$ narrower than 0.6 is due to the delayed turbulent transition of the supersonic jet.[53] The profile of u outside the jet is different between these Mach numbers. Large-scale fluctuations of u are generated at $M_J = 0.6$ (regions A and B), which are often related to large-scale vortices that can induce velocity fluctuations, even outside the jet. On the other hand, u sharply changes across shock-like waves outside the jet at $M_J = 2.6$. These waves begin to appear when turbulence develops via shear instability.[77]

Figure 11 visualizes $\theta = \partial u_j/\partial x_j$ for $M_J = 2.6$ in the same plane as in Fig. 10(b). The shock-like waves outside the jets have large negative θ, which indicates fluid compression. The compressive waves induce a rapid velocity change, which generates small-scale velocity fluctuations outside the jet in Fig. 10(b). Similar pressure waves with strong compression are also found inside the jet. Figure 11(b) illustrates θ in the region outlined in Fig. 11(a). Thin regions with large negative θ appear inside the jet. Figure 11(c) shows the instantaneous velocity u in the same region as Fig. 11(b). At the location of large negative θ, u also exhibits a distinct jump (marked as A).

The velocity jumps due to compressive waves are associated with a large velocity gradient, which affects the flatness of $\partial u'/\partial x$. Figure 12 shows the probability density function (PDF) of $\partial u'/\partial x$ as calculated at $y/H = 3$, which is given with horizontal broken lines in Figs. 10 and 11(a). This location is outside the jet, and the velocity fluctuations are dominated by irrotational fluid motion as induced by the jet for low M_J and by compressive waves for high M_J. Here, $\partial u'/\partial x$ is
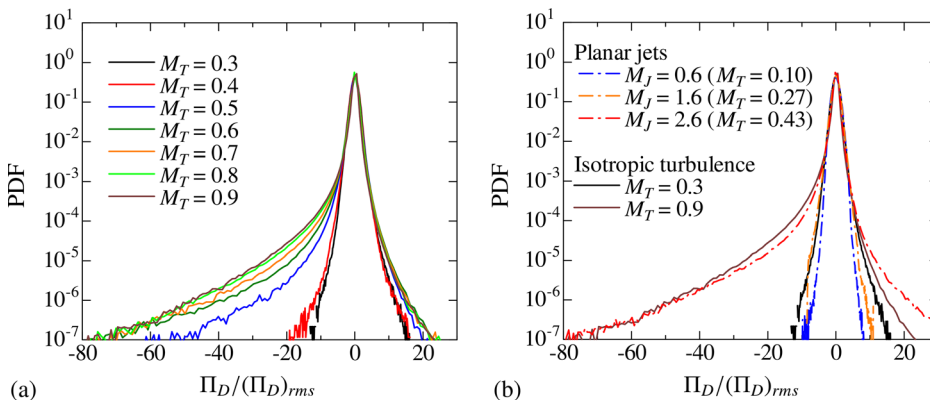

FIG. 13. Probability density function of $\Pi_D/(\Pi_D)_{rms}$ in (a) isotropic turbulence with $Re_{L0} = 900$ and (b) planar jets on the jet centerline at $t/t_r = 26$. The results for isotropic turbulence at $M_T = 0.3$ and 0.9 are also shown in (b).
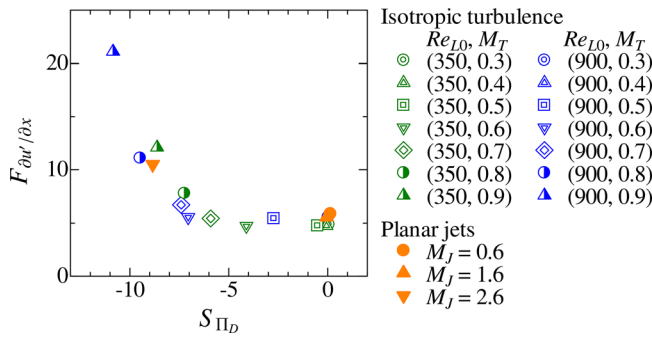
FIG. 14. Relationship between velocity derivative flatness $F_{\partial u'/\partial x}$ and the skewness of Π_D, S_{Π_D}. The DNS results for the planar jets are obtained at $y = 0$ and $t/t_r = 26$.

normalized by the rms fluctuations, $(\partial u'/\partial x)_{rms}$. As M_J increases, the PDF of $\partial u'/\partial x$ deviates from Gaussian. The peak of the PDF at $\partial u'/\partial x \approx 0$ increases with M_J. The semi-log plot in the inset shows that a probability for large negative $\partial u'/\partial x$ increases for larger M_J; thus, the flatness of $\partial u'/\partial x$ increases with M_J. The waves propagate in space and may persist for some time. Therefore, the velocity statistics at the center of the jet at a given time can be influenced by the strong compressive waves that are generated at different locations and times. This wave propagation can make the compressibility effects on the turbulence statistics non-local in space and time. Therefore, deviations of $F_{\partial u'/\partial x}$ from incompressible values may occur at lower M_T in the turbulent jet rather than in statistically steady isotropic turbulence, where M_T does not vary with position or time.

Compressive waves are associated with a pressure increase via fluid compression. The transport equation for kinetic energy $\rho u_i u_i$ can be derived by multiplying Eq. (2) by u_i. The pressure term can be rewritten as $-u_i \partial P/\partial x_i = -\partial u_i P/\partial x_i + P \partial u_i/\partial x_i = D_p + \Pi_D$. The first term D_p represents pressure diffusion, and the second term Π_D is called a pressure–dilatation correlation.[78] The first term on the right-hand side of Eq. (3) is $-\Pi_D$. Therefore, Π_D represents the energy exchange between the kinetic and internal energies. The equation of state, $P = \rho RT$, suggests that $\Pi_D < 0$ increases P via compression

$\partial u_i/\partial x_i < 0$. Figure 13 shows the PDF of Π_D in the isotropic turbulence and at the center of the planar jet. The PDF is negatively skewed for large Mach numbers. This is related to a large negative Π_D in thin wave structures, which occupy a small volume in the flow. The shape of the PDF in Fig. 13(b) is similar for isotropic turbulence with $M_T = 0.9$ and the planar jet with $M_J = 2.6$ despite a smaller M_T in the jet. These results imply that the local M_T is not directly related to the propagation of the shock-like compressive waves. Figure 14 presents the relationship of $F_{\partial u'/\partial x}$ to the skewness of Π_D. The isotropic turbulence with $Re_{L0} = 900$ and the planar jets have $Re_\lambda \approx 100$ for which $F_{\partial u'/\partial x}$ is approximately 6 under incompressible conditions. The results for both flows collapse well, suggesting an increased $F_{\partial u'/\partial x}$ is correlated with an increased $|S_\Pi|$, which is caused by compressive waves with $\Pi_D \ll 0$.

Similar effects for compressive waves may also occur in turbulence as generated by PSJAs. Figure 15(a) (Multimedia view) shows a Schlieren image of the flow as induced by a single PSJA. The camera records the formation of the synthetic jet with a framerate of 28,023 fps and an exposure time of 3.0 μs. The PSJA faces the right side of the figure, and the jet (marked with the broken white lines in the still image) is in the direction during the blowing phase. When a jet issues from the orifice, wave propagation is observed above and below the jet in the video from 2 to 4 s and from 10 to 12 s. The direction of the wave propagation is tilted from the jet direction; for example, the pressure waves below the jet propagate toward the bottom right of the figure. These waves have not been observed in Schlieren images from low-speed synthetic jets,[79] and wave propagation as observed from the PSJA resembles that of a supersonic jet, where the propagation direction is also tilted from the jet axis.[77] Figure 15(b) (Multimedia view) shows a Schlieren image of the turbulence as generated by the eight PSJAs (exp. 1). The images are taken without installing the chamber walls as light diffraction on the side walls makes the image unclear. The camera framerate and the exposure time are 8102 fps and 11 μs, respectively. The center of the visualized domain is slightly higher than the chamber center; thus, the jet formation from the upper PSJAs can be visualized. Wave propagation in turbulence is observed when the jet is issued from the top right at the beginning of the video. The wave pattern is less clear compared with a single PSJA in Fig. 15(a) because the waves propagate in
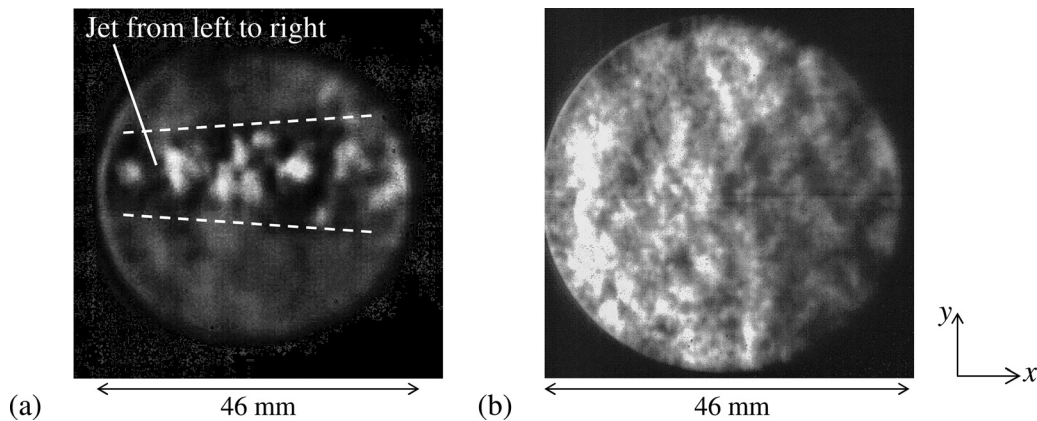

FIG. 15. Schlieren visualization of (a) a synthetic jet generated from a single PSJA and (b) turbulence generated by eight PSJAs in exp. 1. In (a), the jet flow is issued from left to right. Multimedia views: https://doi.org/10.1063/5.0085423.2; https://doi.org/10.1063/5.0085423.3

turbulence with density fluctuations. After the first wave propagation, another jet formation occurs for the PSJA at the bottom right. The waves generated by this jet can also be seen in the video. Wave propagation from the PSJAs cannot be described by the local turbulent Mach number at the chamber center. The strong compressive waves can propagate from the supersonic jets generated by PSJAs and affect the characteristics of fully developed turbulence at the chamber center. The wave propagation from the supersonic synthetic jets can cause the same compressibility effects for low-M_T turbulence with dilatational forcing,[8] which also generates compressive waves at low M_T.

V. CONCLUSIONS

The dependence of the velocity derivative flatness $F_{\partial u'/\partial x}$ on the turbulent Reynolds number Re_λ and turbulent Mach number M_T is examined experimentally for turbulence generated by PSJAs and using

DNS of statistically steady compressible isotropic turbulence and temporally evolving planar jets. The DNS of the isotropic turbulence uses the solenoidal forcing scheme, while the jet velocity ranges from subsonic to supersonic. The PIV measurements and Schlieren flow visualization are conducted for the turbulence chamber with PSJAs. Nearly homogeneous isotropic turbulence is generated at the chamber center from interactions between supersonic synthetic jets.

The relationship between $F_{\partial u'/\partial x}$ and Re_λ has a minimal dependence on the flow in incompressible turbulence. However, $F_{\partial u'/\partial x}$ in turbulence generated by PSJAs is larger than in incompressible turbulence with similar Re_λ. The DNS of the isotropic turbulence and the turbulent planar jets shows that $F_{\partial u'/\partial x}$ becomes larger than incompressible values when the Mach number of the flow is sufficiently high. However, a comparison between the three flows also indicates that the threshold of M_T that characterizes the deviation of $F_{\partial u'/\partial x}$
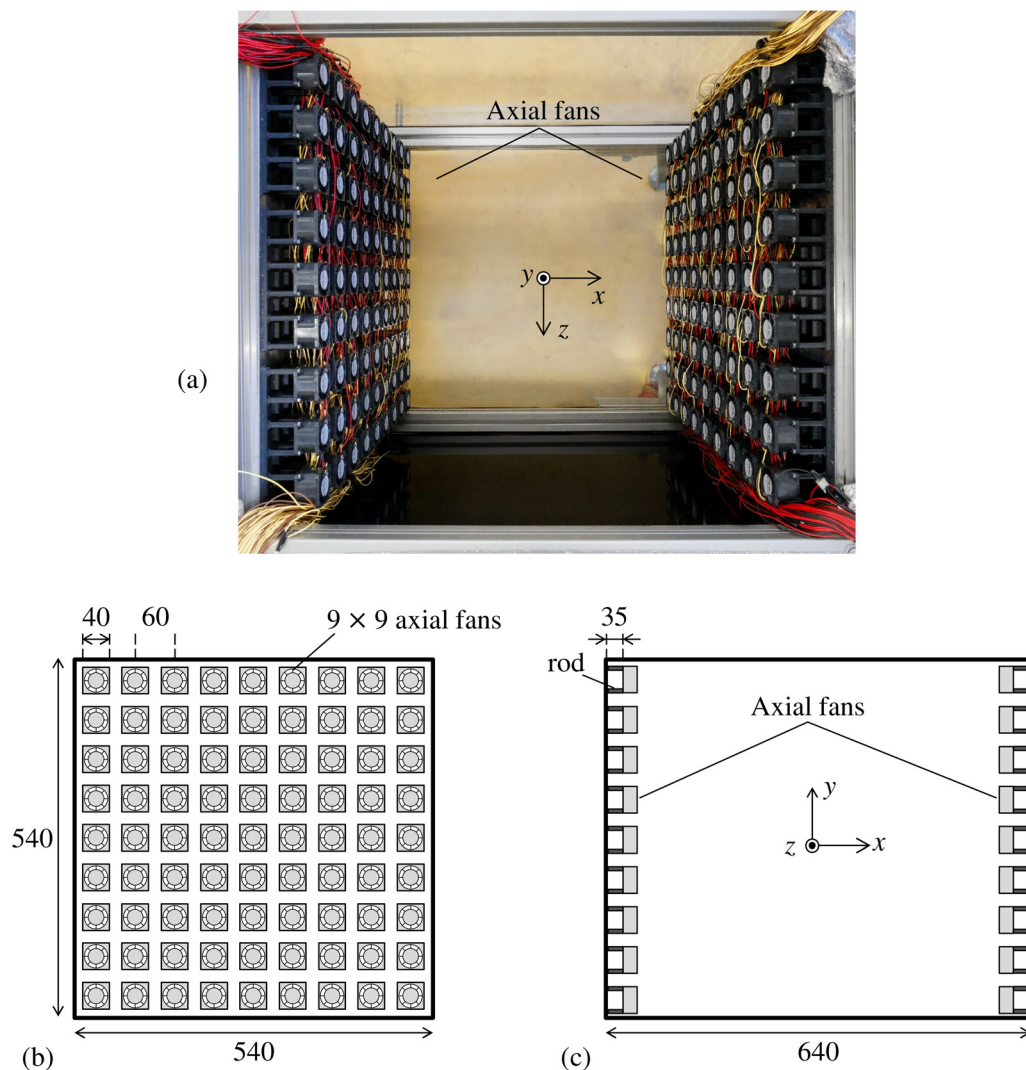

FIG. 16. (a) Photograph of the top view of the multi-fan turbulence chamber (chamber is covered by the top wall during the experiments). Schematics of (b) the arrangement of 81 fans on one side of the chamber and (c) a side view of the turbulence chamber. All dimensions are in mm.

TABLE III. Statistics of the turbulence generated by the fans, where the measurement results at the chamber center.

$\langle u \rangle$ (m/s)	$\langle v \rangle$ (m/s)	u_{rms} (m/s)	v_{rms} (m/s)	u_{rms}/v_{rms}	$\langle \omega_z^2 \rangle / \langle 15(\partial u/\partial x)^2 \rangle$	Re_λ	M_T
−0.17	−0.46	0.61	0.55	1.11	0.30	590	2.9×10^{-3}

from incompressible turbulence depends on the flow. In the isotropic turbulence with a solenoidal linear forcing, $F_{\partial u'/\partial x}$ becomes larger than that for incompressible turbulence when M_T is greater than 0.6, while an increase in $F_{\partial u'/\partial x}$ due to the compressibility effects occurs even for M_T lower than 0.6 in turbulent planar jets and turbulence generated by PSJAs.

The compressibility effect on $F_{\partial u'/\partial x}$ is observed for turbulence generated by PSJAs although $M_T = \mathcal{O}(10^{-2})$ is relatively small. Recent DNS of forced compressible isotropic turbulence indicates that the compressibility effects on turbulence are significant even at $M_T = \mathcal{O}(10^{-2})$ when forcing is applied to a dilatational velocity component.[8] Schlieren flow visualization for PSJAs reveals the propagation of pressure waves when jets are issued from the orifices. These waves are strong enough to cause density fluctuations visible in the Schlieren image. A possible explanation of the large $F_{\partial u'/\partial x}$ in the experiments is the non-local effects of waves as generated by supersonic synthetic jets because they propagate toward the chamber center. The DNS of supersonic planar jets indicates that strong compressive waves induce quasi-discontinuous velocity jumps. These shock-like compressive waves can cause an increased $F_{\partial u'/\partial x}$. In the DNS, the shock-like waves in the jet appear at lower M_T than in isotropic turbulence with the solenoidal forcing scheme. When the waves appear in a flow, the probability distribution of pressure–dilatation correlation, $\Pi_D = P\partial u_i/\partial x_i$ becomes negatively skewed. An increased $F_{\partial u'/\partial x}$ in compressible turbulence is correlated with variations of the skewness of $\Pi_D = P\partial u_i/\partial x_i$. This suggests that an increased $F_{\partial u'/\partial x}$ in the DNS and experiments is caused by wave propagation, which is not directly related to a local value of M_T.

The compressibility effects cause an increased $F_{\partial u'/\partial x}$ from the propagation of compressive waves, which can induce dilatational velocity fluctuations. This is consistent with the compressibility effects for turbulence observed in DNS with dilatational forcing.[8] The dilatational forcing scheme is artificial because it selectively excites dilatational velocity fluctuations. It is unclear whether similar compressibility effects at low M_T are possible in turbulence that is naturally generated. This study with PSJAs provides experimental evidence that supports the numerical finding based on dilatational forcing.[8] The results of the experiments and DNS demonstrate that the turbulence generation process is important for the compressibility effects, which are not solely determined from a local value of M_T.

ACKNOWLEDGMENTS

AUTHOR DECLARATIONS
Conflict of Interest

The authors have no conflicts to disclose.

DATA AVAILABILITY

The data that support the findings of this study are available from the corresponding author upon reasonable request.

APPENDIX: EXPERIMENTS OF INCOMPRESSIBLE TURBULENCE GENERATED BY MULTIPLE FANS

The PIV measurements are gathered for turbulence as generated by multiple fans to provide reference data of the velocity derivative flatness for incompressible turbulence. The multi-fan turbulence chamber (Fig. 16) generates turbulence with multiple DC electric fans and is similar to those used in Refs. 41–43 and 80. Two sets of 9×9 fans (Sanyo Denki, San Ace 40, 9GA0412P3K011) are equipped on opposing surfaces of a rectangular chamber whose inner size is $540 \times 640 \times 540$ mm³. The same fans are used in our previous paper, which tested an in-house color PIV system for the flow induced by the fans.[73] Each fan induces flow with a mean axial velocity of approximately 10 m/s. The fans are fixed by rods with a 35 mm length on aluminum plates with a 10 mm thickness. The side, bottom, and top walls are acrylic plates with a thickness of 3 mm. The rotational speed of fans is 2.2×10^4 rpm, which is measured for each fan using a pulse sensor. Interactions of flow as induced by 182 fans generate turbulence inside the chamber. The coordinate system is also shown in Fig. 16. The direction of the fans is denoted by x, and the vertical and spanwise directions are denoted by y and z, respectively.

The velocity measurements on the x-y plane are conducted at the chamber center with the same PIV system used with the PSJAs. Before the measurements, the chamber is filled with oil mists as generated by a fog generator. The particles are illuminated with a laser from the bottom of the chamber while the camera faces the z direction. The time interval between two laser pulses is $400 \mu s$, and the measurement area is 40×40 mm² around the chamber center. The spatial resolution of 1.7 mm is approximately 6 times the Kolmogorov scale η, and the resolution compared with η is similar to the PSJAs experiments. In each measurement, 150 snapshots of the velocity vectors are acquired, and the experiment is repeated 8 times. The statistics are then calculated with ensemble averages of 1200 snapshots. The statistics obtained at the chamber center are summarized in Table III. The mean velocity is as small as the rms velocity, and large-scale fluctuations are nearly isotropic as confirmed from $u_{rms} \approx v_{rms}$. In incompressible turbulence, the local isotropy at small scales is often assessed with the vorticity variance. For vorticity in the z direction, $\omega_z = \partial v/\partial x - \partial u/\partial y$, the

assumption of local isotropy requires $\langle\omega_z^2\rangle/\langle 15(\partial u/\partial x)^2\rangle = 1/3$ for incompressible turbulence.[64] This relationship is not valid for compressible turbulence because the derivation relies on the continuity equation for incompressible fluids.[81] The present PIV measurement yields $\langle\omega_z^2\rangle/\langle 15(\partial u/\partial x)^2\rangle = 0.30$, which is close to the theoretical value 1/3. Thus, turbulence generated in the chamber is nearly isotropic at both large and small scales. The turbulent Reynolds number Re_λ is as large as those for the PSJAs although u_{rms} is approximately 1/10 of those in the PSJAs. This is due to the large length scales of the turbulence as generated by the fans. The relationship between $F_{\partial u'/\partial x}$ and Re_λ as measured using the PIV shows good quantitative agreement between fan-generated turbulence and previous studies of incompressible turbulence (Fig. 8).

REFERENCES

[1]W. R. Graham, "Boundary layer induced noise in aircraft, Part I: The flat plate model," J. Sound Vib. **192**, 101 (1996).

[2]B. E. Milton and K. Pianthong, "Pulsed, supersonic fuel jets-A review of their characteristics and potential for fuel injection," Int. J. Heat Fluid Flow **26**, 656 (2005).

[3]J. Urzay, "Supersonic combustion in air-breathing propulsion systems for hypersonic flight," Annu. Rev. Fluid Mech. **50**, 593 (2018).

[4]R. M. Crutcher, "What drives star formation?," Astrophys. Space Sci. **292**, 225 (2004).

[5]Y. Sakurai, T. Ishihara, H. Furuya, M. Umemura, and K. Shiraishi, "Effects of the compressibility of turbulence on the dust coagulation process in protoplanetary disks," Astrophys. J. **911**, 140 (2021).

[6]S. B. Pope, *Turbulent Flows* (Cambridge University Press, 2000).

[7]K. R. Sreenivasan and R. A. Antonia, "The phenomenology of small-scale turbulence," Annu. Rev. Fluid Mech. **29**, 435 (1997).

[8]D. A. Donzis and J. P. John, "Universality and scaling in homogeneous compressible turbulence," Phys. Rev. Fluids **5**, 084609 (2020).

[9]T. Watanabe, K. Tanaka, and K. Nagata, "Solenoidal linear forcing for compressible, statistically steady, homogeneous isotropic turbulence with reduced turbulent Mach number oscillation," Phys. Fluids **33**, 095108 (2021).

[10]S. Lee, S. K. Lele, and P. Moin, "Eddy shocklets in decaying compressible turbulence," Phys. Fluids **3**, 657 (1991).

[11]J. R. Ristorcelli and G. A. Blaisdell, "Consistent initial conditions for the DNS of compressible turbulence," Phys. Fluids **9**, 4 (1997).

[12]F. Bataille and Y. Zhou, "Nature of the energy transfer process in compressible turbulence," Phys. Rev. E **59**, 5417 (1999).

[13]R. Samtaney, D. I. Pullin, and B. Kosović, "Direct numerical simulation of decaying compressible turbulence and shocklet statistics," Phys. Fluids **13**, 1415 (2001).

[14]S. Pirozzoli and F. Grasso, "Direct numerical simulations of isotropic compressible turbulence: influence of compressibility on dynamics and structures," Phys. Fluids **16**, 4386 (2004).

[15]K. Lee, S. S. Girimaji, and J. Kerimo, "Effect of compressibility on turbulent velocity gradients and small-scale structure," J. Turbul. **10**, N9 (2009).

[16]J. Larsson, I. Bermejo-Moreno, and S. K. Lele, "Reynolds-and Mach-number effects in canonical shock–turbulence interaction," J. Fluid Mech. **717**, 293 (2013).

[17]J. Ryu and D. Livescu, "Turbulence structure behind the shock in canonical shock–vortical turbulence interaction," J. Fluid Mech. **756**, R1 (2014).

[18]Q. Zhang and Z. Xiao, "Single-particle dispersion in compressible turbulence," Phys. Fluids **30**, 040904 (2018).

[19]J. Wang, T. Gotoh, and T. Watanabe, "Shocklet statistics in compressible isotropic turbulence," Phys. Rev. Fluids **2**, 023401 (2017).

[20]K. Inokuma, T. Watanabe, K. Nagata, A. Sasoh, and Y. Sakai, "Finite response time of shock wave modulation by turbulence," Phys. Fluids **29**, 051701 (2017).

[21]K. Tanaka, T. Watanabe, K. Nagata, A. Sasoh, Y. Sakai, and T. Hayase, "Amplification and attenuation of shock wave strength caused by homogeneous isotropic turbulence," Phys. Fluids **30**, 035105 (2018).

[22]K. Inokuma, T. Watanabe, K. Nagata, and Y. Sakai, "Statistics of overpressure fluctuations behind a weak shock wave interacting with turbulence," Phys. Fluids **31**, 085119 (2019).

[23]Y. P. M. Sethuraman and K. Sinha, "Effect of turbulent Mach number on the thermodynamic fluctuations in canonical shock-turbulence interaction," Comput. Fluids **197**, 104354 (2020).

[24]K. Tanaka, T. Watanabe, and K. Nagata, "Statistical analysis of deformation of a shock wave propagating in a local turbulent region," Phys. Fluids **32**, 096107 (2020).

[25]S. Jagannathan and D. A. Donzis, "Reynolds and Mach number scaling in solenoidally-forced compressible turbulence using high-resolution direct numerical simulations," J. Fluid Mech. **789**, 669 (2016).

[26]M. R. Petersen and D. Livescu, "Forcing for statistically stationary compressible isotropic turbulence," Phys. Fluids **22**, 116101 (2010).

[27]O. San and K. Kara, "Evaluation of Riemann flux solvers for WENO reconstruction schemes: Kelvin–Helmholtz instability," Comput. Fluids **117**, 24 (2015).

[28]M. S. Uberoi and S. Wallis, "Effect of grid geometry on turbulence decay," Phys. Fluids **10**, 1216 (1967).

[29]C. S. Shet, M. R. Cholemari, and S. V. Veeravalli, "Optimizing the performance of an active grid to generate high intensity isotropic free stream turbulence," Phys. Fluids **32**, 095120 (2020).

[30]R. Maryami, S. A. Showkat Ali, M. Azarpeyvand, and A. Afshari, "Turbulent flow interaction with a circular cylinder," Phys. Fluids **32**, 015105 (2020).

[31]Y. Zheng, K. Nagata, and T. Watanabe, "Turbulent characteristics and energy transfer in the far field of active-grid turbulence," Phys. Fluids **33**, 115119 (2021).

[32]M. Dghim, K. Ben Miloud, M. Ferchichi, and H. Fellouah, "Meandering of a wing-tip vortex in a grid-generated turbulent flow," Phys. Fluids **33**, 115131 (2021).

[33]P. J. Zwart, R. Budwig, and S. Tavoularis, "Grid turbulence in compressible flow," Exp. Fluids **23**, 520 (1997).

[34]G. Briassulis, J. H. Agui, and Y. Andreopoulos, "The structure of weakly compressible grid-generated turbulence," J. Fluid Mech. **432**, 219 (2001).

[35]T. Kouchi, M. Iwachido, T. Nakagawa, Y. Nagata, and S. Yanase, "Transverse jet mixing in a supersonic grid turbulence," AIAA Paper No. AIAA 2020-2040, 2020.

[36]N. Manzano-Miura, D. Gloutak, and G. P. Bewley, "Characterization of a turbulent flow with independent variation of Mach and Reynolds numbers," Exp. Fluids **63**, 44 (2022).

[37]J. H. Agui, G. Briassulis, and Y. Andreopoulos, "Studies of interactions of a propagating shock wave with decaying grid turbulence: Velocity and vorticity fields," J. Fluid Mech. **524**, 143 (2005).

[38]G. Fukushima, J. Wei, S. Ogawa, J. Hagiwara, Y. Nakamura, and A. Sasoh, "Losing the shock wave front profile due to interaction with turbulence," Fluid Dyn. Res. **53**, 025504 (2021).

[39]W. Hwang and J. K. Eaton, "Creating homogeneous and isotropic turbulence without a mean flow," Exp. Fluids **36**, 444 (2004).

[40]C. Goepfert, J.-L. Marié, D. Chareyron, and M. Lance, "Characterization of a system generating a homogeneous isotropic turbulence field by free synthetic jets," Exp. Fluids **48**, 809 (2010).

[41]M. Birouk, B. Sarh, and I. Gökalp, "An attempt to realize experimental isotropic turbulence at low Reynolds number," Flow, Turbul. Combust. **70**, 325 (2003).

[42]S. Ravi, S. J. Peltier, and E. L. Petersen, "Analysis of the impact of impeller geometry on the turbulent statistics inside a fan-stirred, cylindrical flame speed vessel using PIV," Exp. Fluids **54**, 1424 (2013).

[43]D. Bradley, M. Lawes, and M. E. Morsy, "Measurement of turbulence characteristics in a large scale fan-stirred spherical vessel," J. Turbul. **20**, 195 (2019).

[44]G. Bellani and E. A. Variano, "Homogeneity and isotropy in a laboratory turbulent flow," Exp. Fluids **55**, 1646 (2014).

[45]D. Carter, A. Petersen, O. Amili, and F. Coletti, "Generating and controlling homogeneous air turbulence using random jet arrays," Exp. Fluids **57**, 189 (2016).

[46]A. Pérez-Alvarado, L. Mydlarski, and S. Gaskin, "Effect of the driving algorithm on the turbulence generated by a random jet array," Exp. Fluids **57**, 20 (2016).

[47]J. F. Krawczynski, B. Renou, and L. Danaila, "The structure of the velocity field in a confined flow driven by an array of opposed jets," Phys. Fluids **22**, 045104 (2010).

[48]K. Yamamoto, T. Watanabe, and K. Nagata, "Turbulence generated by an array of opposed piston-driven synthetic jet actuators," Exp. Fluids **63**, 35 (2022).

[49]T. M. Crittenden and A. Glezer, "A high-speed, compressible synthetic jet," Phys. Fluids **18**, 017107 (2006).

[50]J. L. Gilarranz, L. W. Traub, and O. K. Rediniotis, "A new class of synthetic jet actuators—Part I: Design, fabrication and bench top characterization," ASME J. Fluids Eng. **127**, 367 (2005).

[51]L. W. Traub, M. Sweet, and K. Nilssen, "Evaluation and characterization of a lateral synthetic jet actuator," J. Aircraft **49**, 1039 (2012).

[52]H. Sakakibara, T. Watanabe, and K. Nagata, "Supersonic piston synthetic jets with single/multiple orifice," Exp. Fluids **59**, 76 (2018).

[53]R. Nagata, T. Watanabe, and K. Nagata, "Turbulent/non-turbulent interfaces in temporally evolving compressible planar jets," Phys. Fluids **30**, 105109 (2018).

[54]Y. Tai, T. Watanabe, and K. Nagata, "Modeling of molecular diffusion and thermal conduction with multi-particle interaction in compressible turbulence," Phys. Fluids **30**, 035108 (2018).

[55]S. Gottlieb and C.-W. Shu, "Total variation diminishing Runge-Kutta schemes," Math. Comput. **67**, 73 (1998).

[56]G.-S. Jiang and C.-W. Shu, "Efficient implementation of weighted ENO schemes," J. Comput. Phys. **126**, 202 (1996).

[57]C. A. Kennedy and M. H. Carpenter, "Several new numerical methods for compressible shear-layer simulations," Appl. Numer. Math. **14**, 397 (1994).

[58]Z. Wang, Y. Lv, P. He, J. Zhou, and K. Cen, "Fully explicit implementation of direct numerical simulation for a transient near-field methane/air diffusion jet flame," Comput. Fluids **39**, 1381 (2010).

[59]J. Berland, C. Bogey, and C. Bailly, "Numerical study of screech generation in a planar supersonic jet," Phys. Fluids **19**, 075105 (2007).

[60]X. Zhang, T. Watanabe, and K. Nagata, "Turbulent/nonturbulent interfaces in high-resolution direct numerical simulation of temporally evolving compressible turbulent boundary layers," Phys. Rev. Fluids **3**, 094605 (2018).

[61]Y. Tai, T. Watanabe, and K. Nagata, "Multi-particle models of molecular diffusion for Lagrangian simulation coupled with LES for passive scalar mixing in compressible turbulence," Comput. Fluids **221**, 104886 (2021).

[62]Y. Tai, T. Watanabe, and K. Nagata, "Implicit large eddy simulation of passive scalar transfer in compressible planar jet," Int. J. Numer. Methods Fluids **93**, 1183 (2021).

[63]T. Zhou and R. A. Antonia, "Reynolds number dependence of the small-scale structure of grid turbulence," J. Fluid Mech. **406**, 81 (2000).

[64]T. Zhou, R. A. Antonia, and L. P. Chua, "Flow and Reynolds number dependencies of one-dimensional vorticity fluctuations," J. Turbul. **6**, N28 (2005).

[65]M. Kamruzzaman, L. Djenidi, and R. A. Antonia, "Study of the interaction of two decaying grid-generated turbulent flows," Phys. Fluids **33**, 095122 (2021).

[66]R. A. Antonia and A. J. Chambers, "On the correlation between turbulent velocity and temperature derivatives in the atmospheric surface layer," Boundary-Layer Meteorol. **18**, 399 (1980).

[67]R. M. Kerr, "Higher-order derivative correlations and the alignment of small-scale structures in isotropic numerical turbulence," J. Fluid Mech. **153**, 31 (1985).

[68]A. Y.-S. Kuo and S. Corrsin, "Experiments on internal intermittency and fine-structure distribution functions in fully turbulent fluid," J. Fluid Mech. **50**, 285 (1971).

[69]J. Mi, M. Xu, and T. Zhou, "Reynolds number influence on statistical behaviors of turbulence in a circular free jet," Phys. Fluids **25**, 075101 (2013).

[70]C. W. Van Atta and R. A. Antonia, "Reynolds number dependence of skewness and flatness factors of turbulent velocity derivatives," Phys. Fluids **23**, 252 (1980).

[71]T. Watanabe and K. Nagata, "Integral invariants and decay of temporally developing grid turbulence," Phys. Fluids **30**, 105111 (2018).

[72]Y. Zheng, K. Nagata, and T. Watanabe, "Energy dissipation and enstrophy production/destruction at very low Reynolds numbers in the final stage of the transition period of decay in grid turbulence," Phys. Fluids **33**, 035147 (2021).

[73]K. Aruga, T. Watanabe, and K. Nagata, "Color contamination correction based on light intensity correlation in two-color, double-exposure particle tracking velocimetry," Exp. Fluids **61**, 142 (2020).

[74]N. S. Vaghefi and C. K. Madnia, "Local flow topology and velocity gradient invariants in compressible turbulent mixing layer," J. Fluid Mech. **774**, 67 (2015).

[75]J. W. Nichols, S. K. Lele, F. E. Ham, S. Martens, and J. T. Spyropoulos, "Crackle noise in heated supersonic jets," J. Eng. Gas Turbines Power **135**, 051202 (2013).

[76]C.-C. Ye, P.-J.-Y. Zhang, Z.-H. Wan, D.-J. Sun, and X.-Y. Lu, "Numerical investigation of the bevelled effects on shock structure and screech noise in planar supersonic jets," Phys. Fluids **32**, 086103 (2020).

[77]C. K. W. Tam, "Supersonic jet noise," Annu. Rev. Fluid Mech. **27**, 17 (1995).

[78]S. K. Lele, "Compressibility effects on turbulence," Annu. Rev. Fluid Mech. **26**, 211 (1994).

[79]B. L. Smith and A. Glezer, "The formation and evolution of synthetic jets," Phys. Fluids **10**, 2281 (1998).

[80]E. S. Semenov, "Measurement of turbulence characteristics in a closed volume with artificial turbulence," Combust. Explos. ShockWaves **1**, 57 (1965).

[81]J. O. Hinze, *Turbulence* (McGraw-Hill, New York, 1975).